scientific reports

OPEN

Detection of ultrafast electron energization by whistler-mode chorus waves in the magnetosphere of Earth

S. Kurita[1]✉, Y. Miyoshi[2], S. Saito[3], S. Kasahara[4], Y. Katoh[5], S. Matsuda[6], S. Yokota[7], Y. Kasahara[6], A. Matsuoka[8], T. Hori[2], K. Keika[4], M. Teramoto[9] & I. Shinohara[10]

Electromagnetic whistler-mode chorus waves are a key driver of variations in energetic electron fluxes in the Earth's magnetosphere through the wave-particle interaction. Traditionally understood as a diffusive process, these interactions account for long-term electron flux variations (> several minutes). However, theories suggest that chorus waves can also cause rapid (< 1 s) electron acceleration and significant flux variations within less than a second through a nonlinear wave-particle interaction. Detecting these rapid accelerations has been a great challenge due to a limited time resolution of conventional particle instruments. Here, we employ an analysis technique to enhance the time resolution of the particle measurements, revealing rapid electron flux variations within less than one second associated with chorus waves. This technique exposes short-lived flux increases significantly larger than those observable with the standard time resolution. Our findings indicate that these transient flux variations result from the nonlinear acceleration of electrons induced by the chorus waves, highlighting the importance of nonlinear wave-particle interactions in creating high energy electrons in the Earth's magnetosphere. The same acceleration mechanism should operate in the magnetospheres of Jupiter and Saturn where chorus waves are present, and in laboratory plasma environments when chorus-like waves are excited.

Resonant wave-particle interactions form a crucial aspect in the heating, acceleration, transport, and loss processes of plasma in both space and laboratory environments. Various types of plasma waves significantly influence the dynamics of energetic particle fluxes in the Earth's inner magnetosphere through the wave-particle interactions. Specifically, whistler-mode waves are essential in driving electron dynamics within this region. Whistler mode waves generated by a nonlinear process outside the plasmapause, known as whistler-mode chorus waves, induce the pitch angle scattering of electrons ranging from a few keV to tens of keV. This scattering is associated with the generation of diffuse and pulsating auroras[1–7]. Furthermore, chorus waves can resonate with relativistic electrons, facilitating the creation of MeV electrons in the outer radiation belt and causing their precipitation into the Earth's upper atmosphere[7–13].

Previous modeling studies on wave-induced particle flux variations have primarily utilized quasi-linear diffusion theory to describe changes in the energy and pitch angle of resonant particles due to wave-particle interactions[14,15]. These models have elucidated the long-term evolution of radiation-belt electron fluxes during geomagnetic disturbances[16,17] and have successfully explained the evolution of pitch angle distributions of low-energy electrons during their convective transport in the inner magnetosphere[18]. Additionally, the computation of quasi-linear diffusion coefficients has been instrumental in identifying the dominant generation mechanism of diffuse auroras[1,19].

[1]Research Institute for Sustainable Humanosphere, Kyoto University, Uji 611-0011, Japan. [2]Institute for Space-Earth Environmental Research, Nagoya University, Nagoya 464-8601, Japan. [3]National Institute of Information and Communications Technology, Tokyo 184-8795, Japan. [4]Graduate School of Science, The University of Tokyo, Tokyo 113-0033, Japan. [5]Graduate School of Science, Tohoku University, Sendai 980-8578, Japan. [6]Graduate School of Natural Science and Technology, Kanazawa University, Kanazawa 920-1192, Japan. [7]Graduate School of Science, Osaka University, Toyonaka 560-0043, Japan. [8]Graduate School of Science, Kyoto University, Kyoto 606-8502, Japan. [9]Graduate School of Engineering, Kyushu Institute of Technology, Iizuka 820-8501, Japan. [10]Institute of Space and Astronautical Science, Japan Aerospace Exploration Agency, Sagamihara 252-5210, Japan. ✉email: kurita.satoshi.8x@kyoto-u.ac.jp

However, nonlinear wave-particle interactions have also been recognized for their role in rapid changes in energy and pitch angle changes[20–22], which quasi-linear diffusion theory does not account for[23–34]. Recent satellite observations exhibit the presence of large-amplitude and coherent whistler-mode waves in the Earth's inner magnetosphere[35–37], alongside particle flux variations coincident with large-amplitude whistler-mode waves[38–43]. Those observations underscore the significant impact of nonlinear wave-particle interactions on particle dynamics in the inner magnetosphere.

The Medium Energy Particle Instrument-electron analyzer (MEP-e)[44] onboard the Arase satellite[45] has recorded deformations in electron distribution functions associated with the appearance of a large amplitude upper-band chorus within 30 s[46], closely resembling the "flux burst event" observed by the Van Allen probes[47]. It is revealed that resonance with the upper-band chorus presumably caused the observed electron flux variations. Subsequent data-driven test particle simulations based on the Arase observations indicated that the electron flux variations within 30 s are attributed to the nonlinear phase trapping of electrons by the upper-band chorus[48]. A comparison between the observation and the test particle simulations suggests that the nonlinear wave-particle interaction is essential for explaining the short timescale of the observed flux variations.

Investigating the signature of nonlinear wave-particle interactions in the MEP-e measurements presents a difficulty due to the nominal observation cadence of ~ 8 s, which is insufficient to detect such interactions. We aim to capture this signature by analyzing higher temporal flux variations, improving upon the analysis conducted by Kurita et al.[46], which utilized the MEP-e data at its nominal time resolution. We utilized the measurement scheme of MEP-e to generate a time series of pitch-angle-resolved electron fluxes at a time cadence much shorter than the nominal one. The methodology shown in this study is applicable to other instruments that employ a similar observational approach to the MEP-e.

Arase observation

The MEP-e instrument measures electrons ranging from 7 to 87 keV across 16 energy steps and features a disk-like shaped field of view encompassing 2π radians with 16 detectors. The spin period of the satellite (~ 8 s) is segmented into 32 phases, with a 16-step energy scan executed in each spin phase. By virtue of the disk-like field of view and the observation scheme of MEP-e, electron pitch angle distributions across 16 directions are attainable with a time cadence of ~ 250 ms (calculated as ~ 8 s divided by 32 spin phases). Note that, within each spin phase, the 16-step energy scan is made with an accumulation time for electrons at each energy step of ~ 15.6 ms (250 ms divided by 16 steps). We refer to the high temporal resolution pitch angle distribution obtained at a cadence of ~ 250 ms as the "250 ms pitch angle distribution". In case of the 250 ms pitch angle distribution, the coverage of pitch angle is highly dependent on the angle between the normal direction of the MEP-e field of view and the background magnetic field direction, which is simultaneously measured by the Magnetic Field Experiment (MGF)[49]. As the satellite rotates, the angle between the normal direction and magnetic field changes periodically, so does the pitch angle coverage accordingly.

The 250 ms pitch angle distributions are computed during the "flux burst event" that has originally been reported by Kurita et al.[46]. During the event, the 8-s averaged pitch angle distributions show distinct changes associated with the appearance of upper-band chorus waves. This change was characterized by the flux enhancement of electrons in the energy range of 17–30 keV with the pitch angles of 60°-80° and 100°-120°.

An overview of this event is shown in Fig. 1. Figures 1a and 1b show the frequency-time spectra of the electric field and magnetic field fluctuations in the frequency range of 64 Hz to 20 kHz computed by Onboard Frequency Analyzer (OFA)[50] with a time cadence of 1 s, which is a part of Plasma Wave Experiment (PWE)[51]. The electric and magnetic field signals were measured using wire probe antennas[52] and magnetic search coils[53]. The local electron cyclotron frequency and its half were computed from the MGF measurements, and are shown as solid and dotted magenta lines, respectively. Figures 1a and 1b represent that whistler-mode wave activity is present almost all the time in the electric field, while only a few bursts can be seen in the magnetic field component during this time interval. This feature suggests that the whistler-mode waves, except the bursts, are quasi-electrostatic, suggesting that the wave normal angles close to the resonance cone. Figure 1c shows the energy-time spectrogram of electrons measured by MEP-e, and omnidirectional fluxes are color-coded in Fig. 1c. The timing of the flux burst event is indicated by the black dotted vertical line in Fig. 1. The flux enhancement observed by MEP-e, shown in Fig. 1c, corresponds well with the appearance of an intense upper-band chorus, as shown in Figs. 1a and 1b.

Figure 2 shows the property of whistler-mode chorus waves associated with the flux burst event. Here we show two types of data product computed by OFA: survey mode power spectra (OFA-SPEC), which is shown in Figs. 1a and 1b, and spectral matrices (OFA-SPEC) of wave magnetic fields. OFA-SPEC is obtained by computing the Fast Fourier Transform (FFT) of a 15.625 ms waveform segment measured every 1 s. OFA-MATRIX is generated from the ensemble average of FFT spectra computed from four consecutive 15.625 ms waveform segments captured every 8 s.

Figures 2a and 2b show the dynamics spectra of OFA-SPEC and a sum of diagonal components (i.e., total wave magnetic field power) of OFA-MATRIX. During this time interval, OFA-SPEC was operated to compute the total wave magnetic field power. Figure 2c shows the wave normal angle derived from OFA-MATRIX, applying the singular value decomposition method[54]. Black dashed lines in Figs. 2a, 2b, and 2c represent half the electron gyrofrequency computed from the magnetic field intensity measured by MGF. Figure 2d represents time series of integrated wave power in the frequency range from 0.5 f_{ce} to 0.8 f_{ce} computed from OFA-SPEC (back solid line with plus symbol) and OFA-MATRIX (magenta dashed line with diamond symbol). Note that the timing of the data aquation corresponds to the center of the spectra in Figs. 2a, 2b, and 2c.

The upper-band chorus waves during this time interval have wave normal angles lower than 30 degrees with the maximum band-integrated amplitude exceeding 200 pT. Around 19:21:33 UT, the wave amplitude computed from OFA-SPEC is smaller by a factor of ~ 3 compared to that derived from OFA-MATRIX. This feature can be

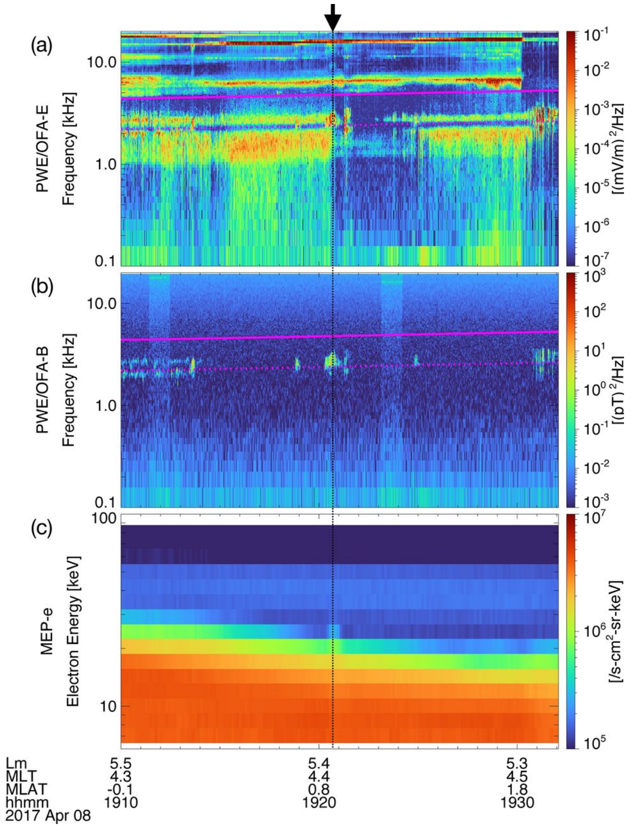

Fig. 1. Overview of plasma wave activity and electron flux variations observed by the Arase satellite during the flux burst event. From top to bottom: Frequency-time spectra of (**a**) electric and (**b**) magnetic field fluctuations of plasma waves observed by PWE/OFA, (c) energy-time spectrogram of electrons in the energy range from 7–80 keV observed by MEP-e.

explained by the fact that OFA-MATRIX uses four times longer waveforms in computation compared to OFA-SPEC. Considering that OFA-MATRIX is the average of four FFT spectra, the maximum amplitude within the 15.625 waveform segment which is not measured by OFA-SPEC, would be much larger than 150 pT. It is also expected that wave amplitude varies significantly within short time intervals less than a few tens of milliseconds. Unfortunately, high-time resolution waveforms are not available during this time interval, so we cannot discuss fine-scale spectral structures and short-term variations in wave amplitudes and propagation properties less than a second in detail.

In order to clarify that the observed upper-band waves are responsible for the electron acceleration during the flux burst event, changes in electron phase space density (PSD) as a function of energy and pitch angle before and during the flux burst event are examined. Figures 3a and 3b show the PSD distributions before and during the flux burst event, respectively, together with resonance curves (white lines) and a series of diffusion curves (black dotted lines). The resonance curves are represented assuming the first-order cyclotron resonance of parallel propagating whistler mode waves with electrons. We used the lower-cutoff (0.5 f_{ce}, solid lines) and upper-cutoff (0.66 f_{ce}, dashed lines) frequencies of the upper-band chorus wave at 19:21:33 UT to represent the resonance curves. Based on the Arase satellite observation, the ratio of plasma frequency to the electron cyclotron frequency of 3.4 is used to compute the resonance curves and diffusion curves. The PSD of 24.5 keV electrons around the pitch angle range of 60°to 80°and 100°to 120° is clearly enhanced during the flux burst event compared to the initial distribution. The regions of the enhanced PSD correspond well to where resonant interactions of electrons with the upper-band chorus waves are expected, indicating that the observed upper-band chorus waves contribute to the electron acceleration. The electron flux enhancement is also observed in the energy range from 17–30 keV, where the resonant interaction with the upper-band chorus is expected[46].

Figures 4a and 4b present the 8-s averaged and 250 ms pitch angle distributions of 24.5 keV electrons during the flux burst event. Although the spin dependence of the pitch angle coverage is apparent in Fig. 4b, the 250 ms pitch angle distributions during this event encompass the pitch angle range where flux enhancement is observed. While the 8-s averaged distributions show a 30-s-long moderate flux burst, the 250 ms pitch angle distributions reveal many significant transient flux increases within the pitch angle range of 70° to 80° are embedded in the moderate flux enhancement.

The flux increase observed in the 250 ms pitch angle distributions is further examined by comparing it with the variations in the 8-s averaged flux within the pitch angle range of 60° to 80° and 100° to 120°. Figures 4c and 4d display the electron flux averaged over these pitch angle ranges, respectively. Black lines indicate the flux

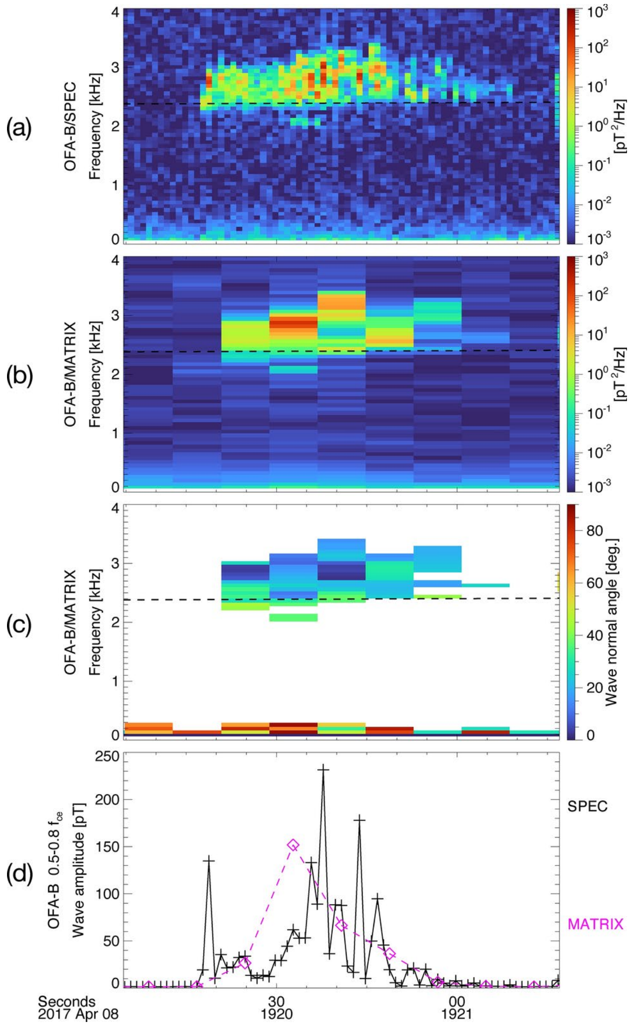

Fig. 2. Property of the chorus waves associated with the flux burst event. (**a**) Frequency-time spectra of wave magnetic field with a time cadence of 1 s computed by OFA (OFA-SPEC). (**b**) Frequency spectra of the sum of the diagonal component of the spectral matrices computed by OFA (OFA-MATRIX) whose time cadence is 8 s. (**c**) Wave normal angle of the waves derived from the OFA-MATRIX dataset applying the singular value decomposition technique[54]. (**d**) Time series of wave amplitude computed from OFA-SPEC (black) and OFA-MATRIX (magenta) integrated over 0.5 to 0.8 times of the local electron gyrofrequency.

averaged over ~ 8 s, and blue dots represent the flux measured at ~ 250 ms intervals. Black vertical bars indicate the standard deviation of the 8-s averaged flux $\boldsymbol{\sigma_G}$, which is calculated using the 250 ms flux every 8 s as:

$$\boldsymbol{\sigma_G} = \sqrt{\frac{\sum_{i=0}^{N-1} (\boldsymbol{j_i} - \boldsymbol{J})^2}{\boldsymbol{N}}} \tag{1}$$

$$\boldsymbol{J} = \frac{1}{\boldsymbol{N}} \sum_{i=0}^{N-1} \boldsymbol{j_i} \tag{2}$$

where j_i denotes the individual 250 ms flux measurements and N indicates the number of measurements in the specified pitch angle range during the 8-s time interval. The subscript G indicates that the standard deviation is computed assuming that the data follow a Gaussian distribution.

Both before and after the flux burst event, the 250 ms electron flux closely followed the variations in the 8-s averaged flux as indicated by the small standard deviation. During the flux burst event, the 250 ms flux exhibited significant deviations from the 8-s average flux, particularly at the onset of the event. The 250 ms flux demonstrated substantial increases relative to the 8-s average, resulting the large standard deviation during the flux burst event. The standard deviation was observed to be larger during the flux burst event than periods before

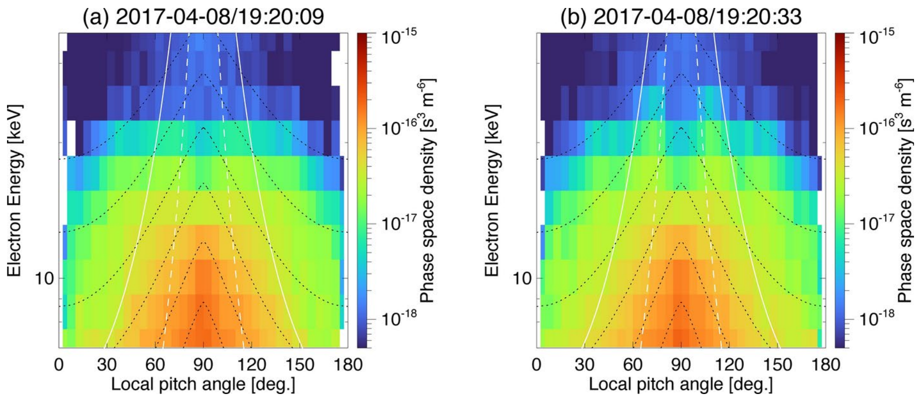

Fig. 3. Comparison of electron phase space density distribution in the energy and pitch angle domain before and during the flux burst event. (**a**) Distribution of electron phase space density as a function of energy and pitch angle just before the flux burst event. (**b**) Same as (**a**) except the time interval when the flux increase takes place in association with the appearance of the upper-band chorus waves. The white solid and dashed lines represent the resonance curves at 0.5 f_{ce} and 0.66 f_{ce} computed under the assumption of the first-order cyclotron resonance between electrons and parallel-propagating whistler-mode waves. These frequencies are adopted from the Arase observation. Black dotted lines denote the series of the diffusion curves.

and after the flux burst event. The 250 ms flux was analyzed in comparison with the 8-s averaged flux also for 20.5 keV electrons, revealing similar features to those observed with 24.5 keV electrons (not shown).

Discussion and Summary

The standard deviation of the electron fluxes, calculated over 8-s interval, was greater during the flux burst event than before and after it. This increase in standard deviation may have been caused by the short-lived, significant flux increase during the event. Additionally, random fluctuations due to the counting statistics might also contribute to the larger standard deviation observed during the flux burst event. This possibility is quantitatively evaluated as follows.

Given the counting statistics, a large average count could lead to a larger standard deviation, as the standard deviation in a Poisson distribution is the square root of the average count, C. Therefore, the coefficient of variation (CV), which normalizes the standard deviation by the average value, can be expressed as follows:

$$CV_P = \frac{\sqrt{C}}{C} = \frac{1}{\sqrt{C}} \tag{3}$$

The parameter CV_p can be obtained from the electron count detected by MEP-e in the specified time interval and pitch angle range. The subscript P denotes that the parameter is computed, assuming that the measurement follows a Poisson distribution. Under the assumption that the electron flux in the specified time interval and pitch angle range follows a Gaussian distribution, the parameter CV can be derived from the standard deviation σ_G and average flux J in the specified time interval and pitch angle range evaluated as

$$CV_G = \frac{\sigma_G}{J} \tag{4}$$

According to Eq. (3), the counting statistics suggest that an increase in electron count, which corresponds to a higher electron flux, results in a decrease in CV_p. As the electron count increases, the Poisson distribution approaches a Gaussian distribution. Consequently, it is anticipated that both CV_p and CV_G would decrease during the flux burst event if the random fluctuations predominantly influence the high temporal flux variations. Comparing CV_p with CV_G offers insights into whether the observed flux variations are attributable to random fluctuations.

Figure 5a displays the 8-s averaged pitch angle distributions of 24.5 keV electrons during the flux burst event interval. The enhancement of flux in the oblique pitch angle range coincides with the flux burst occurrence. In Fig. 5b, the magenta and blue lines represent CV_p and CV_G, respectively, for 24.5 keV electrons within the 60°-80° range of the pitch angle. Before and after the flux burst event, the temporal variation in CV_G closely mirrors that of CV_p despite minor fluctuations in CV_G. These parameters are quite similar during the period of high flux, which is attributed to the Poisson distribution approximating a Gaussian distribution when electron counts are high. During the flux burst event, CV_p decreased as expected due to the electron flux enhancement, whereas CV_G increased. This discrepancy between these parameters indicates that the observed flux variation is not merely due to random fluctuations from the counting statistics but is considered to be physically significant. Hence the error estimation performed here strongly suggests that the high temporal variation observed in the flux burst event originates from the physical processes that cause rapid and substantial flux enhancement.

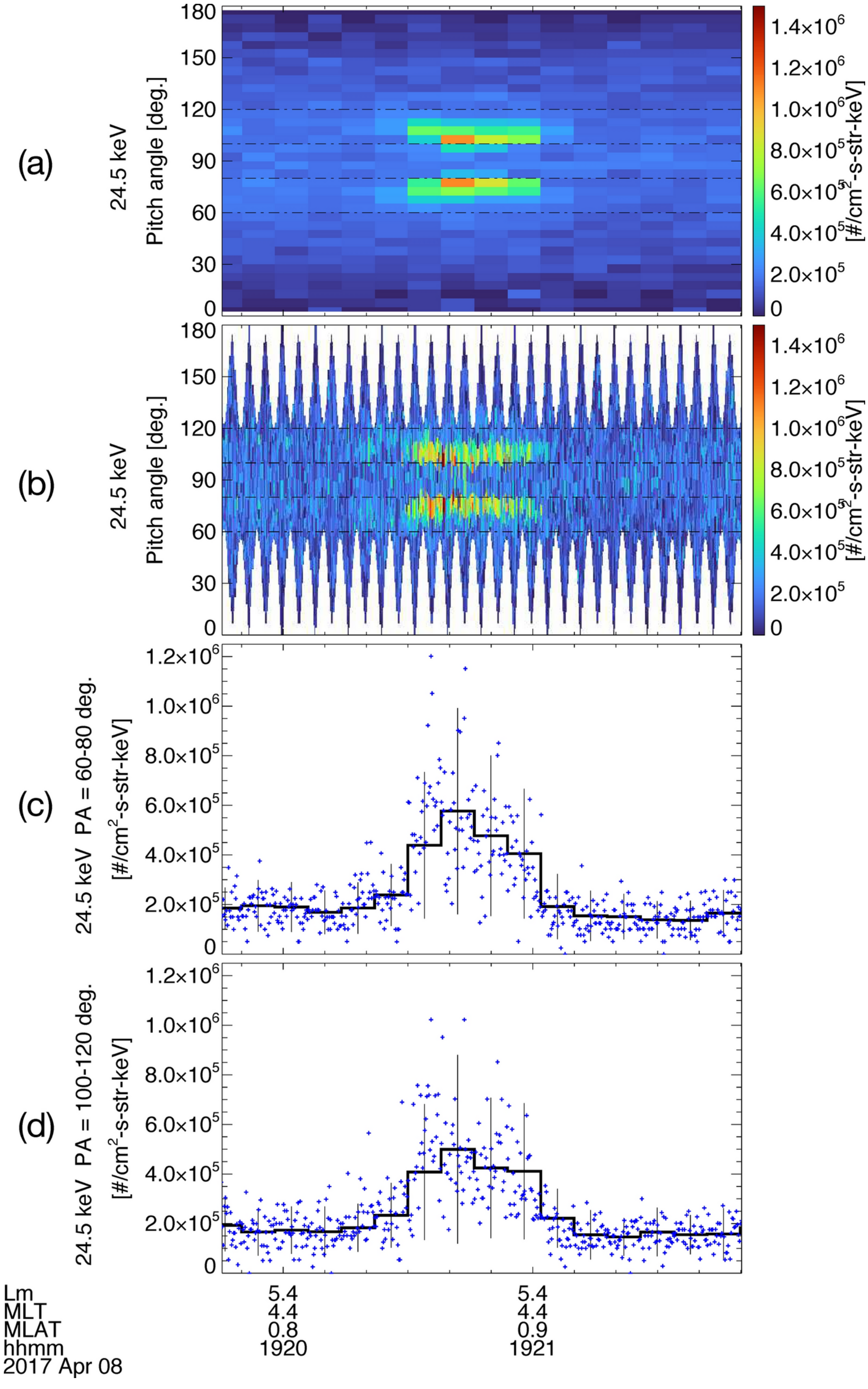

Fig. 4. Detailed view of the time variations in pitch angle distributions of 24.5 keV electrons during the flux burst event. (**a**) Pitch angle distribution derived from the MEP-e measurement averaged over one spin period (~8 s). (**b**) Pitch angle distribution with a time cadence of ~250 ms derived from the MEP-e, utilizing the measurement scheme. (**c**) and (**d**) Variations in electron fluxes in the pitch angle range from 60° to 80° and from 100° to 120°, respectively. Black thick lines in (**c**) and (**d**) indicate the one spin average, and blue dots represent ~250 ms flux variations. The thin black vertical bars denote the standard deviation computed from electron fluxes in one spin period.

The observation of the flux burst event by MEP-e onboard the Arase satellite, using a unique analysis technique, provides new insights into the wave-particle interactions. The 250 ms pitch angle distributions reveal that rapid flux fluctuations are embedded in the flux burst event. When comparing the 250 ms electron flux with the 8-s average, the fluctuations can be categorized into short-lived large flux increases that deviate from the 8-s

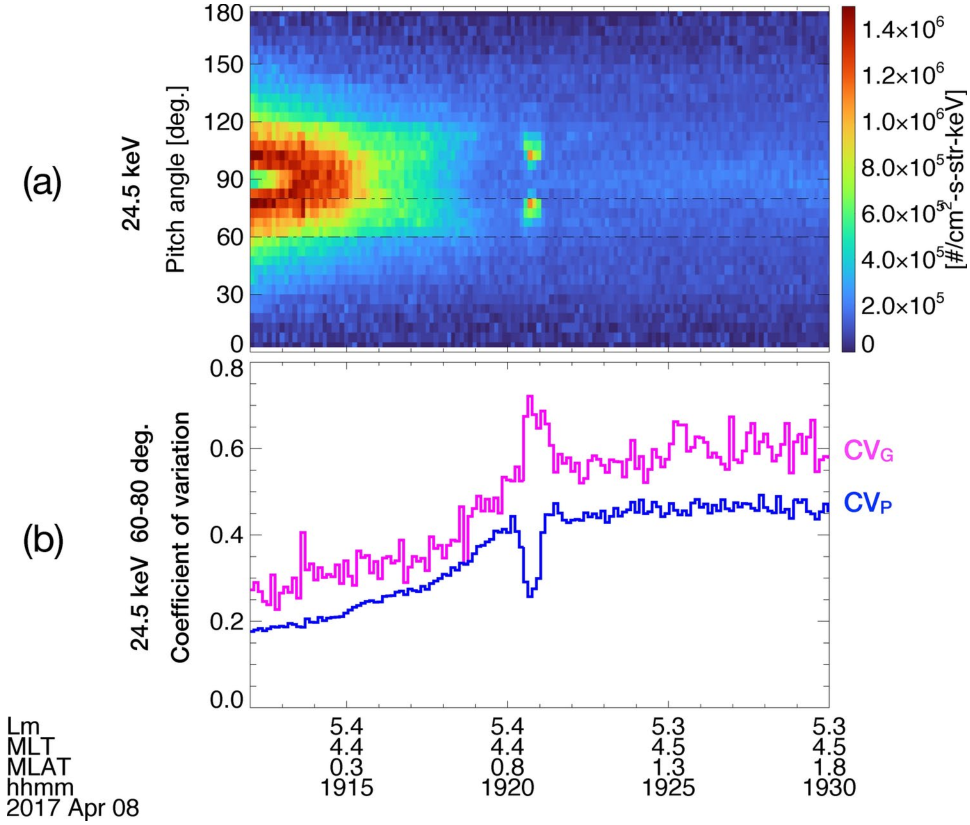

Fig. 5. Coefficients of variation during the flux burst event computed in different ways. (**a**) Pitch angle distribution of 24.5 keV electrons averaged over one spin period around the time interval of the flux burst event. Dotted-dash horizontal lines show pitch angles of 60° and 80°. (**b**) Coefficients of variations, which is defined as the standard deviation divided by the average for 24.5 keV electron measurements in the pitch angle range from 60° to 80°. Blue line indicates the result computed from electron fluxes in one spin period. Magenta line represents the result assuming that the electron count follows the Poisson distribution.

average and the 30-s-long moderate flux enhancement. The short-lived large flux increases were qualitatively similar to those caused by the electron acceleration due to chorus waves through nonlinear phase trapping. Nonlinear phase trapping accelerates electrons for very brief intervals, typically on the order of subseconds, although the occurrence of such nonlinear acceleration is rare due to the limited range of the phase-trapping conditions. The moderate flux enhancement may be interpreted as diffusive acceleration resulting from the energy transfer between the chorus waves and electrons outside the trapping condition. However, we should note that high temporal flux variations arise even under the quasi-linear diffusion regime if wave amplitudes significantly vary within a short time interval. The rapid amplitude variation results in a large change in diffusion coefficients, possibly causing rapid flux variations. Since the OFA measurements suggest a significant time variation in the wave amplitude of the upper-band chorus waves, we need to consider whether the quasi-linear diffusion approximation can explain the observed flux variations or not.

Based on the quasi-linear diffusion approximation, we estimated the time scale for electron transport from lower energy and pitch angle to higher energy and pitch angle along the diffusion curve. As shown in Fig. 4b, MEP-e captures the largest flux enhancement of 24.5 keV electrons at a pitch angle of ~ 80° around the beginning of the flux burst event. The electrons are expected to be transported from the lower energy range since such a high-flux level close to the enhanced one is not observed in the 24.5 keV channels during this time interval, indicating that pitch angle diffusion in the same energy channel is not a plausible explanation for the largest flux enhancement. Figure 3b shows that the diffusion curve, which passes through the pitch angle of ~ 80° in the 24.5 keV channel, lies in the pitch angle range of 60°-70° in the 20.5 keV channel. Electrons in that energy and pitch angle range can be the source populations of the enhanced electron PSD in the 24.5 keV channel. To explain the observed feature, electrons would need to be diffused 10°-20° in pitch angle, during which MEP-e scans the 24.5 keV energy channel (15.6 ms). The pitch angle diffusion coefficient $D_{\alpha\alpha}$ for the upper-band chorus during this event was estimated to be an order of 10^{-2} (rad^2/s)[48], which results in the pitch angle change of ~ 1° for 15.6 ms. The change in pitch angle is estimated to be smaller compared to the expected one from the MEP-e observation, suggesting that it is hard to explain the observed flux enhancement by the diffusive process. Thus, the significant short-lived flux enhancement during the flux burst event provides observational evidence that the flux burst event resulted from the nonlinear acceleration of electrons by chorus waves, as demonstrated by test particle simulations[48].

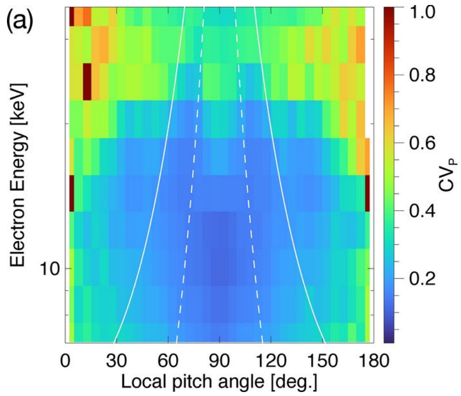

Fig. 6. Distribution of Coefficients of variation in energy and pitch angle domain during the flux burst event. (**a**) Distribution of coefficients of variation as a function of energy and pitch angle computed from the inverse value of the square root of count for 8-s interval (Poisson distribution assumption). (**b**) Same as (**a**) except for coefficients of variation computed from the standard deviation and average flux for 8-s interval using the 250 ms flux (Gaussian distribution assumption). The resonance curves shown Fig. 2a and 2b are overplotted in these figures.

The limited accumulation time and field-of-view of MEP-e might contribute to the apparently short-lived observation of the flux increase. The MEP-e observation scheme accumulates electron counts for ~ 15.6 ms every ~ 250 ms at each energy step, resulting in a gap of ~ 234 ms in measurements for a specific energy range. During the accumulation of one energy step, only a very limited area of the entire solid angle is measured by MEP-e. This measurement limitation could explain the short-lived nature of the flux increase observed in the 250 ms pitch angle distribution.

Although the rapid flux variations might be caused by the instrumental issue, the distribution of CV_P and CV_G in the energy and pitch angle domain, which are shown in Figs. 6a and 6b, respectively, gives a clue to consider the electron acceleration and pitch angle scattering through the wave-particle interaction. The resonance curves shown in Figs. 2a and 2b are also overlayed in Figs. 6a and 6b. Paying attention to the regions bounded by the resonance curves of 0.5 f_{ce} and 0.66 f_{ce}, the large difference between CV_G and CV_P only appears along the resonance curves of the upper-cutoff frequency in 20.5 keV and 24.5 keV channels. In the region of the large CV_G compared to CV_P, the flux variations cannot be explained by the random fluctuation, suggesting the presence of physical processes causing the high temporal flux variations in the large CV_G region. The localized enhancements of CV_G imply that electrons are intermittently and selectively transported into the higher energy and pitch angle range. The selective transport of electrons toward higher energy and pitch angle is like the behavior of electron transport by nonlinear phase-trapping[23,24]. It should be noted that complicated behavior of nonlinearly resonant electrons is possible under wave amplitude modulations[29,32], which may contribute to the significant flux variations causing large CV_G compared to CV_P.

The analysis of the statistical parameters CV_G and CV_P can be performed using a dataset obtained by particle detectors which uses the measurement principle similar to MEP-e. Not only electron data but also ion data obtained by other satellite missions such as Cluster, THEMIS, and Van Allen Probes would be used to investigate rapid flux variations caused by some physical mechanisms using the technique shown in this study.

In summary, this study offers new insights into nonlinear wave-particle interactions through the unique analysis technique of electron observation, suggesting that nonlinear acceleration by chorus waves is significant in the Earth's inner magnetosphere. The substantial flux increase during brief intervals supports the occurrence of nonlinear electron acceleration by the upper-band chorus waves. The analysis technique introduced in this study could be applied to other particle instruments to investigate rapid particle flux change associated with plasma wave activity. Additionally, applying this analysis to the test particle simulations of Saito et al.[48] could validate the interpretation presented here, which is proposed as an avenue for future research.

Data availability
The science data of the ERG (Arase) satellite used in this study were obtained from the ERG Science Center operated by ISAS/JAXA and ISEE/Nagoya University (https://ergsc.isee.nagoya-u.ac.jp/index.shtml.en)[55]. The MEP-e Level 2 v1.01[56] and MGF Level 2 v3.04[57] data were analyzed to generate the energy-time spectrogram and pitch angle distributions. The PWE/OFA-SPEC Level 2 v2.03[58] data were used to show the frequency-time spectrograms of the electromagnetic fields. We also used the Level 2 v04 definitive orbit data of the Arase satellite[59].

Code availability
The Space Physics Environment Data Analysis Software (SPEDAS) software package[60], including ERG plug-in tools (https://ergsc.isee.nagoya-u.ac.jp/erg_socware/erg_plugin/), is publicly available at http://themis.ssl.berkeley.edu/software.shtml and can be used without any restrictions.

Received: 24 August 2024; Accepted: 21 November 2024
Published online: 14 January 2025

References

1. Thorne, R. M., Ni, B., Tao, X., Horne, R. B. & Meredith, N. P. Scattering by chorus waves as the dominant cause of diffuse auroral precipitation. *Nature* **467**, 934–936 (2010).
2. Nishimura, Y. et al. Multievent study of the correlation between pulsating aurora and whistler mode chorus emissions. *J. Geophys. Res.* **116**, A11221. https://doi.org/10.1029/2011JA016876 (2011).
3. Kasahara, S. et al. Pulsating aurora from electron scattering by chorus waves. *Nature* https://doi.org/10.1038/nature25505 (2018).
4. Miyoshi, Y. et al. Time of flight analysis of pulsating aurora electrons, considering wave-particle interactions with propagating whistler mode waves. *J. Geophys. Res.* **115**, A10312. https://doi.org/10.1029/2009JA015127 (2010).
5. Miyoshi, Y. et al. Relation between energy spectra of pulsating aurora electrons and frequency spectra of whistler-mode chorus waves. *J. Geophys. Res.* **120**, 7728–7736. https://doi.org/10.1002/2015JA021562 (2015).
6. Jaynes, A. N. et al. Correlated Pc4–5 ULF waves, whistler-mode chorus, and pulsating aurora observed by the Van Allen Probes and ground-based systems. *J. Geophys. Res. Space Physics* **120**, 8749–8761. https://doi.org/10.1002/2015JA021380 (2015).
7. Miyoshi, Y., S. Oyama, S. Saito, H. Fujiwara, R. Kataoka, Y. Ebihara, C. Kletzing, G. Reeves, O. Santolik, M. Cliverd, C. Rodger, E. Turunen, and F. Tsuchiya, Energetic electron precipitation associated with pulsating aurora: EISCAT and Van Allen Probes observations, J. Geophys. Res., 120, https://doi.org/10.1002/2014JA020690, 2015b.
8. Lorentzen, K. R., Blake, J. B., Inan, U. S. & Bortnik, J. Observations of relativistic electron microbursts in association with VLF chorus. *J. Geophys. Res.* **106**, 6017 (2001).
9. O'Brien, T.P., et al. Energization of relativistic electrons in the presence of ULF power and MeV microbursts: evidence for dual ULF and VLF acceleration. *J. Geophys. Res.* **108**, 1329. https://doi.org/10.1029/2002JA009784 (2003).
10. Kurita, S., Miyoshi, Y., Blake, J. B., Reeves, G. D. & Kletzing, C. A. Relativistic electron microbursts and variations in trapped MeV electron fluxes during the 8–9 October 2012 storm: SAMPEX and Van Allen Probes observations. *Geophys. Res. Lett.* **43**, 3017–3025. https://doi.org/10.1002/2016GL068260 (2016).
11. Kurita, S., Miyoshi, Y., Blake, J. B. & Friedel, R. H. W. Response of relativistic electron microbursts to the arrival of high-speed solar wind streams and its relation to flux variation of trapped radiation belt electrons. *Journal of Geophysical Research: Space Physics* **123**, 7452–7461. https://doi.org/10.1029/2018JA025675 (2018).
12. Miyoshi, Y., S. Saito, S. Kurita, K. Asamura, K. Hosokawa, T. Sakanoi, T. Mitani, Y. Ogawa, S. Oyama, F. Tsuchiya, S. L. Jones, A. N. Jaynes, and J. B. Blake, Relativistic Electron Microbursts as High Energy Tail of Pulsating Aurora Electrons, Geophys. Res. Lett., 47 https://doi.org/10.1029/2020GL090360,2020.
13. Miyoshi, Y. et al. Penetration of MeV electrons into the mesosphere accompanying pulsating aurorae. *Scientific Reports* **11**, 13724. https://doi.org/10.1038/s41598-021-92611-3 (2021).
14. Kennel, C. F. & Petschek, H. E. Limit on stably trapped particle fluxes. *J. Geophys. Res.* **71**(1), 1–28. https://doi.org/10.1029/JZ071i001p00001 (1966).
15. Lyons, L. R. & Thorne, R. M. Equilibrium structure of radiationbelt electrons. *J. Geophys. Res.* **78**, 2142–2149 (1973).
16. Shprits, Y. Y., Subbotin, D. & Ni, B. Evolution of electron fluxes in the outer radiation belt computed with the VERB code. *J. Geophys. Res.* **114**, A11209. https://doi.org/10.1029/2008JA013784 (2009).
17. Glauert, S. A., Horne, R. B. & Meredith, N. P. Three-dimensional electron radiation belt simulations using the BAS Radiation Belt Model with new diffusion models for chorus, plasmaspheric hiss, and lightning-generated whistlers. *J. Geophys. Res. Space Physics* **119**, 268–289. https://doi.org/10.1002/2013JA019281 (2014).
18. Tao, X. et al. Evolution of electron pitch angle distributions following injection from the plasma sheet. *J. Geophys. Res.* **116**, A04229. https://doi.org/10.1029/2010JA016245 (2011).
19. Ni, B., R. M. Thorne, N. P. Meredith, R. B. Horne, and Y. Y. Shprits (2011), Resonant scattering of plasma sheet electrons leading to diffuse auroral precipitation: 2. Evaluation for whistler mode chorus waves, J. Geophys. Res., 116, A04219, https://doi.org/10.1029/2010JA016233.
20. Dysthe, K. B. Some studies of triggered whistler emissions. *J. Geophys. Res.* **76**(28), 6915–6931. https://doi.org/10.1029/JA076i028p06915 (1971).
21. Inan, U. S., Bell, T. F. & Helliwell, R. A. Nonlinear pitch angle scattering of energetic electrons by coherent VLF waves in the magnetosphere. *J. Geophys. Res.* **83**(A7), 3235–3253. https://doi.org/10.1029/JA083iA07p03235 (1978).
22. Bell, T. F. The nonlinear gyroresonance interaction between energetic electrons and coherent VLF waves propagating at an arbitrary angle with respect to the Earth's magnetic field. *J. Geophys. Res.* **89**(A2), 905–918. https://doi.org/10.1029/JA089iA02p00905 (1984).
23. Bortnik, J., Thorne, R. M. & Inan, U. S. Nonlinear interaction of energetic electrons with large amplitude chorus. *Geophys. Res. Lett.* **35**, L21102. https://doi.org/10.1029/2008GL035500 (2008).
24. Katoh, Y., Omura, Y. & Summers, D. Rapid energization of radiation belt electrons by nonlinear wave trapping. *Ann. Geophys.* **26**, 3451–3456. https://doi.org/10.5194/angeo-26-3451-2008 (2008).
25. Omura, Y., Furuya, N. & Summers, D. Relativistic turning acceleration of resonant electrons by coherent whistler mode waves in a dipole magnetic field. *J. Geophys. Res.* **112**, A06236. https://doi.org/10.1029/2006JA012243 (2007).
26. Furuya, N., Omura, Y. & Summers, D. Relativistic turning acceleration of radiation belt electrons by whistler mode chorus. *J. Geophys. Res.* **113**, A04224. https://doi.org/10.1029/2007JA012478 (2008).
27. Saito, S., Miyoshi, Y. & Seki, K. Rapid increase in relativistic electron flux controlled by nonlinear phase-trapping of whistler chorus elements. *J. Geophys. Res.* **121**, 6573–6589. https://doi.org/10.1002/2016JA022696 (2016).
28. Allanson, O., Watt, C. E. J., Allison, H. J., & Ratcliffe, H. (2021). Electron diffusion and advection during nonlinear interactions with whistler-mode waves. *Journal of Geophysical Research: Space Physics*, 126, e2020JA028793. https://doi.org/10.1029/2020JA028793.
29. Allanson, O. et al. The challenge to understand the zoo of particle transport regimes during resonant wave-particle interactions for given survey-mode wave spectra. *Front. Astron. Space Sci.* **11**, 1332931. https://doi.org/10.3389/fspas.2024.1332931 (2024).
30. Albert, J. M., Artemyev, A., Li, W., Gan, L. & Ma, Q. Analytical results for phase bunching in the pendulum model of wave-particle interactions. *Front. Astron. Space Sci.* **9**, 971358. https://doi.org/10.3389/fspas.2022.971358 (2022).
31. Artemyev, A. V., Mourenas, D., Zhang, X.-J., & Vainchtein, D. (2022). On the incorporation of nonlinear resonant wave-particle interactions into radiation belt models. *Journal of Geophysical Research: Space Physics*, 127, e2022JA030853. https://doi.org/10.1029/2022JA030853.
32. Gan, L., Li, W., Ma, Q., Artemyev, A. V., & Albert, J. M. (2022). Dependence of nonlinear effects on whistler-mode wave bandwidth and amplitude: A perspective from diffusion coefficients. *Journal of Geophysical Research: Space Physics*, 127, e2021JA030063. https://doi.org/10.1029/2021JA030063
33. Saito, S., and Y. Miyoshi (2022), Butterfly distribution of relativistic electrons driven by parallel propagating lower band whistler chorus waves, Geophys. Res. Lett., 49, e2022GL099605, https://doi.org/10.1029/2022GL099605.
34. Santolík, O., Gurnett, D. A., Pickett, J. S., Parrot, M. & Cornilleau-Wehrlin, N. Spatio-temporal structure of storm-time chorus. *J. Geophys. Res.* **108**(A7), 1278. https://doi.org/10.1029/2002JA009791 (2003).
35. Santolík, O., Kletzing, C. A., Kurth, W. S., Hospodarsky, G. B. & Bounds, S. R. Fine structure of large-amplitude chorus wave packets. *Geophys. Res. Lett.* **41**, 293–299. https://doi.org/10.1002/2013GL058889 (2014).

36. Cully, C. M., Bonnell, J. W. & Ergun, R. E. THEMIS observations of long-lived regions of large-amplitude whistler waves in the inner magnetosphere. *Geophys. Res. Lett.* **35**, L17S16. https://doi.org/10.1029/2008GL033643 (2008).
37. Cattell, C. et al. Discovery of very large amplitude whistler-mode waves in Earth's radiation belts. *Geophys. Res. Lett.* **35**, L01105. https://doi.org/10.1029/2007GL032009 (2008).
38. Kersten, K. et al. Observation of relativistic electron microbursts in conjunction with intense radiation belt whistler-mode waves. *Geophys. Res. Lett.* **38**, L08107. https://doi.org/10.1029/2011GL046810 (2011).
39. Foster, J. C. et al. Prompt energization of relativistic and highly relativistic electrons during a substorm interval: Van Allen Probes observations. *Geophys. Res. Lett.* **41**, 20–25. https://doi.org/10.1002/2013GL058438 (2014).
40. Agapitov, O. V., Artemyev, A. V., Mourenas, D., Mozer, F. S. & Krasnoselskikh, V. Nonlinear local parallel acceleration of electrons through Landau trapping by oblique whistler mode waves in the outer radiation belt. *Geophys. Res. Lett.* **42**, 10140–10149. https://doi.org/10.1002/2015GL066887 (2015).
41. Foster, J. C. et al. Van Allen Probes observations of prompt MeV radiation belt electron acceleration in nonlinear interactions with VLF chorus. *J. Geophys. Res. Space Physics* **122**, 324–339. https://doi.org/10.1002/2016JA023429 (2017).
42. Zhang, X. J. et al. Superfast precipitation of energetic electrons in the radiation belts of the Earth. *Nat Commun* **13**, 1611. https://doi.org/10.1038/s41467-022-29291-8 (2022).
43. Olifer, L., Morley, S. K., Ozeke, L. G., Mann, I. R., Kalliokoski, M. M. H., Henderson, M. G., et al. (2024). Rapid acceleration bursts in the Van Allen radiation belt. *Journal of Geophysical Research: Space Physics*, 129, e2024JA032544. https://doi.org/10.1029/2024JA032544
44. Kasahara, S. et al. Medium-Energy Particle experiments - electron analyser (MEP-e) for the Exploration of energization and Radiation in Geospace (ERG) mission. *Earth, Planets and Space,* https://doi.org/10.1186/s40623-018-0847-z (2018).
45. Miyoshi Y, Shinohara I, Takashima T, Asamura K, Higashio N, Mitani T, Kasahara S, Yokota S, Kazama Y, Wang S-Y, Tam SW, Ho, P.T.P, Kasahara, Y, Kasaba Y, Yagitani S, Matsuoka A, Kojima H, Katoh H, Shiokawa K, Seki K, Geospace Exploration Project ERG, Earth Planets Space, 70:101, https://doi.org/10.1186/s40623-018-0862-0, 2018.
46. Kurita, S. et al. Deformation of electron pitch angle distributions caused by upper band chorus observed by the Arase satellite. *Geophysical Research Letters* **45**, 7996–8004. https://doi.org/10.1029/2018GL079104 (2018).
47. Fennell, J. F. et al. Van Allen Probes observations of direct wave-particle interactions. *Geophys. Res. Lett.* **41**, 1869–1875. https://doi.org/10.1002/2013GL059165 (2014).
48. Saito, S., Kurita, S., Miyoshi, Y., Kasahara, S., Yokota, S., Keika, K., et al. (2021). Data-driven simulation of rapid flux enhancement of energetic electrons with an upper-band whistler burst. *Journal of Geophysical Research: Space Physics*, 126, e2020JA028979. https://doi.org/10.1029/2020JA028979.
49. Matsuoka, A. et al. The ARASE(ERG) magnetic field investigation, Earth. *Planets and Space* **70**, 43. https://doi.org/10.1186/s40623-018-0800-1 (2018).
50. Matsuda, S. et al. Onboard Software of Plasma Wave Experiment aboard Arase: Instrument Management and Signal Processing of Waveform Capture/Onboard Frequency Analyzer. *Earth, Planets and Space,* https://doi.org/10.1186/s40623-018-0838-0 (2018).
51. Kasahara, Y. et al. The Plasma Wave Experiment (PWE) on board the Arase (ERG) satellite. *Earth, Planets and Space,* https://doi.org/10.1186/s40623-018-0842-4 (2018).
52. Kasaba, Y. et al. Wire Probe Antenna (WPT) and Electric Field Detector (EFD) of Plasma Wave Experiment (PWE) aboard the Arase satellite: specifications and initial evaluation results. *Earth, Planets and Space* **69**(1), 174. https://doi.org/10.1186/s40623-017-0760-x (2017).
53. Ozaki, M. et al. Magnetic Search Coil (MSC) of Plasma Wave Experiment (PWE) aboard the Arase (ERG) satellite. *Earth, Planets and Space,* https://doi.org/10.1186/s40623-018-0837-1 (2018).
54. Santolík, O., Parrot, M. & Lefeuvre, F. Singular value decomposition methods for wave propagation analysis. *Radio Sci.* **38**(1), 1010. https://doi.org/10.1029/2000RS002523 (2003).
55. Miyoshi, Y., T. Hori, M. Shoji, M. Teramoto, T-F. Chang, T. Segawa, N. Umemura, S. Matsuda, S. Kurita, K. Keika, Y. Miyashita, K. Seki, Y. Tanaka, N. Nishitani, S. Kasahara, S. Yokota, A. Matsuoka, Y. Kasahara, K. Asamura, T. Takashima, and I. Shinohara, The ERG Science Center, Earth, Planets, Space., 70:96, https://doi.org/10.1186/s40623-018-0867-8, 2018.
56. Kasahara, S., S. Yokota, T. Hori, K. Keika, Y. Miyoshi, and I. Shinohara, The MEP-e instrument Level-2 3-D flux data of Exploration of energization and Radiation in Geospace (ERG) Arase satellite, https://doi.org/10.34515/DATA.ERG-02000, 2018c.
57. Matsuoka, A., M. Teramoto, S. Imajo, S. Kurita, Y. Miyoshi, and I. Shinohara, The MGF instrument Level-2 spin-averaged magnetic field data of Exploration of energization and Radiation in Geospace (ERG) Arase satellite, https://doi.org/10.34515/DATA.ERG-06001, 2018b.
58. Kasahara, Y., H. Kojima, S. Matsuda, M. Ozaki, S. Yagitani, M. Shoji, S. Nakamura, M. Kitahara, Y. Miyoshi, and I. Shinohara, The PWE/OFA instrument Level-2 power spectrum data of Exploration of energization and Radiation in Geospace (ERG) Arase satellite, https://doi.org/10.34515/DATA.ERG-08000, 2018b.
59. Y. Miyoshi, I. Shinohara and C.-W. Jun, The Level-2 orbit data of Exploration of energization and Radiation in Geospace (ERG) Arase satellite, https://doi.org/10.34515/DATA.ERG-12000, 2018.
60. Angelopoulos, V. et al. The Space Physics Environment Data Analysis System (SPEDAS). *Space Sci. Rev.* **215**, 9. https://doi.org/10.1007/s11214-018-0576-4 (2019).

Acknowledgements
This study was supported by Grant-in-Aid for Scientific Research Grant Numbers 20H01959, 22K03699, 23K25925, 23H01229, and 23H05429 of the Japan Society for Promotion of Science (JSPS). The authors would like to extend sincere thanks to all members of the ERG project, the ERG Science Center, and contributors to the SPEDAS software. We would like to acknowledge Editage (www.editage.jp) for English language editing.

Author contributions
S.K. identified the event, analysed the data set, and wrote the paper. Y.M., S.S., Y.K. and S.M. discussed the event. S.K. provided MEP-e data with S.Y., T.H., and K.K. and discussed the event and interpretation. Y.K. provided PWE data. A.M. and M.T. provided MGF data. I.S. oversaw the ERG project. All authors reviewed the manuscript.

Funding
Japan Society for the Promotion of Science, 20H01959, Japan Society for the Promotion of Science, 22K03699, Japan Society for the Promotion of Science, 23K25925, Japan Society for the Promotion of Science, 23H01299, Japan Society for the Promotion of Science, 23H05429.

Declarations

The authors declare no competing interests.

Additional information

Correspondence and requests for materials should be addressed to S.K.